
Article:
Yu, Y., Krynkin, A. and Horoshenkov, K.V. orcid.org/0000-0002-6188-0369 (2024) Modal coupling analysis of the acoustic wave scattering from blockage in a pipe. Journal of Sound and Vibration, 588. 118522. ISSN 0022-460X

https://doi.org/10.1016/j.jsv.2024.118522

Journal of Sound and Vibration 588 (2024) 118522

Contents lists available at ScienceDirect

Journal of Sound and Vibration

journal homepage: www.elsevier.com/locate/jsvi

Modal coupling analysis of the acoustic wave scattering from blockage in a pipe

Yicheng Yu *, Anton Krynkin, Kirill V. Horoshenkov

Department of Mechanical Engineering, University of Sheffield, Mappin Street, Sheffield S1 3JD, UK

ARTICLE INFO

Keywords:
Blockage
Cylindrical pipe
Wave scattering
Mode coupling
Trapped mode

ABSTRACT

Acoustic sensing system deployed on an autonomous platform (also referred to as robot) for accurate condition monitoring and fault detection in pipes requires the knowledge of wave scattering from various in-pipe faults or the robot itself. Existing solutions to estimate wave scattering tend to either be constrained to the plane wave regime or be computationally expensive outside this range. There has been a lack of work to apply analytical modal coupling methods to study wave scattering from a non-symmetric cross-sectional change in a pipe beyond the plane wave regime. This paper proposes an efficient three-dimensional (3D) modal coupling method to predict wave scattering from a cross-sectional change in a pipe in the frequency range beyond the plane wave regime. The trapped modes induced by a 3D axisymmetric or non-axisymmetric cross-sectional change in an air-filled pipe are estimated using modal coupling analysis. The derived analytical model is validated against numerical simulations and measurements. It agrees with a finite element simulation with Comsol Multiphysics in the $0.01<kR<4$ frequency range (k being the wavenumber and R being the pipe radius) within 15 %, but it is approximately 600 times faster than the Comsol simulation making it attractive for the deployment on sensors with limited computer power that can be used for autonomous inspection of buried pipes.

1. Introduction

The introduction of pipe inspection robots marks a significant milestone in the monitoring of sewage and water distribution networks, facilitating the pre-emptive identification of imperfections and reducing the likelihood of severe breakdowns and environmental pollution. Autonomous robots can carry sensors to work in buried pipes for acoustic condition monitoring and fault detection. These inspection robots offer the opportunity to capitalise on recent advances in acoustic and ultrasonic sensing techniques [1,2]. Acoustic methods have been investigated for blockage detection and condition assessment in sewage pipes in the past decades [3]. Compared with traditional visual closed-circuit television (CCTV) inspection methods, acoustic methods are very attractive because they have much further detection range, less power consumption, and less computation cost. Acoustically reflective artefacts including blockages can be localised remotely with respect to the robot position using the time delay of acoustic echoes measured with a microphone [4]. Recently, Yu et al. [5,6] proposed to use a microphone array on a robotic platform to detect, localise and classify the blockage or lateral connection with the sparse representation and support vector machine methods. Understanding acoustic wave scattering from blockages and other artifacts typically found in sewer pipes is important to support the development of robust localisation and classification algorithm that can be deployed on autonomous robots. Usually, finite element methods (FEM) are

* Corresponding author.
E-mail address: Yicheng.Yu@sheffield.ac.uk (Y. Yu).

https://doi.org/10.1016/j.jsv.2024.118522
Received 6 December 2023; Received in revised form 15 May 2024; Accepted 16 May 2024
Available online 18 May 2024

adopted to predict the acoustic scattering by an arbitrarily shaped artefact in a pipe [5,7]. However, this approach is too computationally expensive to deploy on an autonomous robot with limiting computing resources and power where robust computationally efficient methods are needed to support blockage localisation and classification. This paper proposes a new analytical approach to predict acoustic wave scattering from a cross-sectional change in an air-filled pipe that is computationally efficient to work on a robot with a limited computer power. This work also helps training new machine learning methods to detect faults in a pipe with acoustic data.

In the previous study [5], simulations on the acoustic wave scattering from blockage/lateral connections were implemented using finite element method in Comsol Multiphysics, which is computationally expensive (more than 10 h for the frequency range 100–5000 Hz in a 150 mm diameter pipe with 20 Hz steps). This work also demonstrates that a considerable library of acoustical signatures for many types of in-pipe artefacts (e.g. greater than 1000) were required to train machine learning models. It is unlikely to be practical to generate enough training samples using the FEM because of the massive computational time and power required (more than 10^4 h). In response to this a computationally efficient analytical model is proposed.

Another problem with acoustic methods is that a robot in a pipe occupies a finite volume and represents itself an acoustic scatterer to result in Bound State in the Continuum (BIC) [8]. In this case acoustic waves remain localised in the form of the so-called acoustic "trap modes" [9] even though they coexist with a continuous spectrum of radiating waves that can carry energy away [8]. An acoustic source mounted on the robot can be affected by these trapped modes so that its emission will depend on the robot shape and proximity of the robot to any imperfections in the pipe geometry.

Hein et al. [9] used numerical method to analyse acoustic resonances and trapped modes in waveguides with sphere or cylinder as an acoustic scatterer inside. The numerical solution obtained in [9] is in close agreement with the analytical solution derived by Linton and McIver [10]. However, the work by Linton and McIver [10] assumes the acoustic pressure is zero at infinite distance for the analysis of the eigenmode problem to obtain the trapped modes only, whereas the propagating modes are neglected. This limits the application of the analytical model derived in [10] so that our study addresses the problem of acoustic wave for remote pipe inspection and defects detection in which both the propagating modes and trapped modes should be considered. This study builds up on some related work, e.g. an analytical method developed for the two-dimensional (2D) axisymmetric modal coupling analysis [11–13]. It makes use of the concept of non-Hermitian Hamiltonian to estimate the trapped modes of acoustic resonator with an expanded cavity. A three-dimensional non-axisymmetric waveguide case study was also investigated by Lyapina et al. [14] for a cylindrical resonator in the form of an expanded cavity connecting two uniform waveguides. However, to the best of authors' knowledge, there has been no work to propose a computationally efficient analytical method to predict acoustic wave scattering, particularly in application to reflection/transmission from an axisymmetric/non-axisymmetric 2D/3D blockage (shrunk cavity) in an acoustic waveguide beyond the plane wave regime. In response to that, we propose an application of the modal coupling to analytically resolve acoustic wave scattering from a cross-sectional reduction in a cylindrical pipe caused by a 3D axisymmetric or non-axisymmetric blockage. This approach is also expanded to characterise the acoustic response due to a point source excitation at the BIC regime which is applicable and important for the quantification of the robot body impact in the pipe on the quality of acoustic sensing.

The structure of this paper is organised as follows. Section 2 discusses the theory of mode coupling between the cavity and the infinite waveguide. The derivative of trapped modes, acoustic response corresponding to point source excitation, reflection/transmission coefficient are also discussed in Section 2 subsequently. The simulation results of analytical and numerical solution of the trapped modes induced by the axisymmetric/non-axisymmetric blockage/robot are presented in Section 3.1 and Section 3.2, where acoustic response corresponding to the point source excitation is also discussed. In Section 3.3, the analytical solution of reflection/transmission coefficient of non-axisymmetric blockage is validated against a numerical simulation and experimental data.

2. Theory

In a practical pipe environment, a blockage or robot's body (an artefact) can be of random shape making it difficult to define theoretically the acoustic coupling between the artefact's shape and the waveguide. Numerical methodologies, such as the Finite Element Method (FEM) [5], or semi-analytical approaches [15], may be employed to address this issue but with expensive computational costs. Therefore, blockages are usually simplified with specific shapes, e.g. "half-moon" at the bottom of the pipe [16]. This approximation facilitates an accurate theoretical representation of the artefact's impact on the acoustic field, especially at lower frequencies where the wavelength significantly exceeds the dimensions of the blockage/robot artefact (more than 10 times) rendering such simplifications valid for practical calculations. It is common to deploy sensors for fault detection and condition monitoring in the pipe on a robotic system that is usually located at the centre (e.g. [17]) of the pipe cross-section or at the bottom (e.g. [2,5]) of the pipe. Therefore, the effect of the shape of the robot can also be modelled as an axisymmetric body in the middle of the pipe's cross-section. Both artefacts are characteristic for a 3D cylindrical pipe used in this paper (as shown in Fig. 1).

A blockage with a relatively large cross-section (e.g. above 0.5 area ratio between the blockage and pipe cross-sectional areas) has a strong sound reflection that is relatively straightforward to detect and localise compared to a relatively small blockage [3]. The detection of a smaller blockage is more challenging but important because it enables the water utility to remove it at a relatively low cost and before it will have developed into a larger blockage causing the pipe to lose most of its hydraulic capacity. The autonomous robot carrying the sensor for pipe inspection should also be relatively small with respect to the pipe diameter for its effective, scalable, and versatile operation underground [2,5]. Therefore, in this paper, the analytical model is mainly focused on in-pipe artefacts with a relatively small area ratio that is less than 0.3.

The acoustic impedance of a blockage is another parameter that can affect acoustic scattering. In this paper, blockage/robot is assumed as rigid (the normal derivative of the acoustic pressure at a boundary is zero) so that the effect of the acoustic impedance is

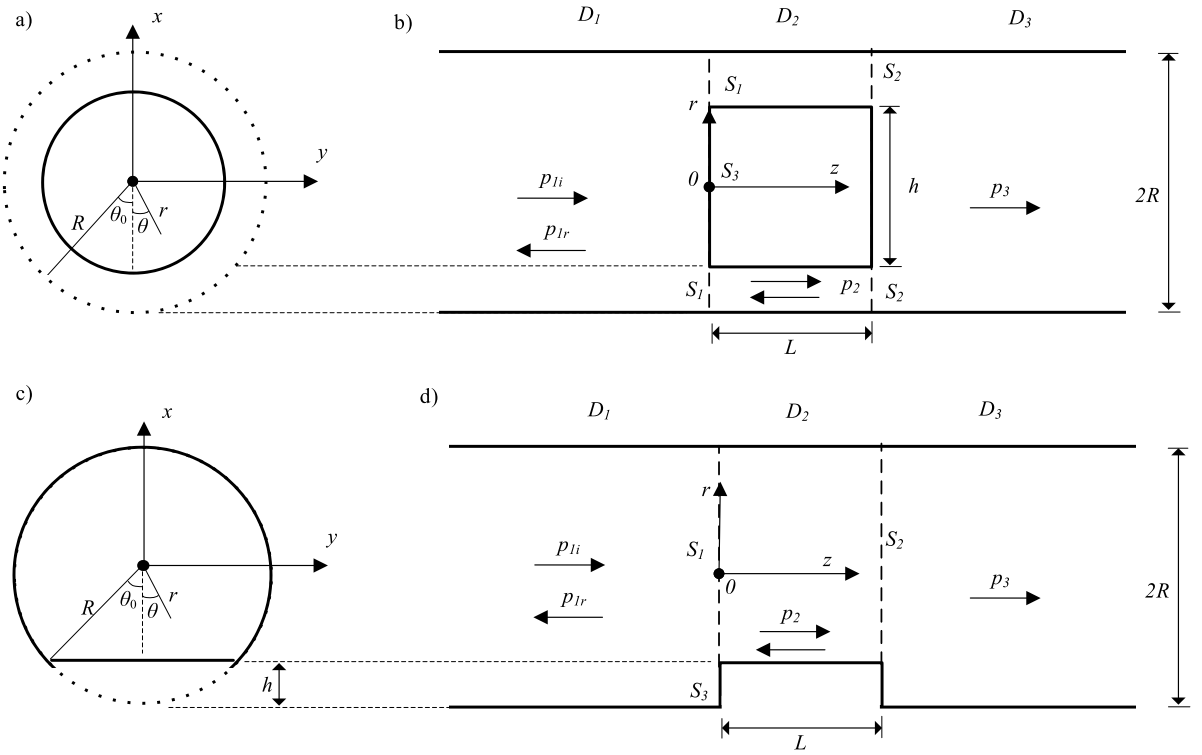

Fig. 1. An illustration of a 3D cylindrical pipe with a blockage: (a) cross-section of the axisymmetric blockage area; (b) side view of the 3D cylindrical axisymmetric pipe; (c) cross-section of the non-axisymmetric blockage area; (d) side view of the 3D cylindrical non-axisymmetric pipe.

ignored. This assumption can be justified by the fact that a majority of blockages in real sewer pipes are either fats or porous media saturated by water. The characteristic impedance of these substances is at least an order of magnitude greater than that of air filling the pipe above the flow of water.

2.1. Modal coupling theory

Assuming the time harmonic dependence in the form of $\exp(-i\omega t)$ throughout the paper, the sound pressure field is governed by the inhomogeneous Helmholtz equation [18]:

$$(\nabla^2 + k_0^2)p = -i\rho_0\omega Q_s(\omega)\delta(\mathbf{r}_s, \mathbf{r}_r), \tag{1}$$

where δ denotes the Dirac function defining a point source excitation, $\mathbf{r}_s$ is the coordinates of the point source, $Q_s(\omega)$ a point source strength, ρ_0 is the density of fluid in the pipe (air), ω is the radial frequency, $\nabla^2 = \frac{1}{r}\frac{\partial}{\partial r}\left(r\frac{\partial}{\partial r}\right) + \frac{1}{r^2}\frac{\partial^2}{\partial\theta^2} + \frac{\partial^2}{\partial z^2}$ is the Laplace operator and $\mathbf{r}_r = (r,\theta,z)$, is the coordinate of the receiver point. In the above equations $k_0 = \omega/c_0$ is the wavenumber in a free field where c_0 is sound velocity in air.

In the semi-infinite domain D_1 (see Fig. 1), the acoustic pressure is given by:

$$p_1 = p_{1i} + p_{1r} = \sum_{m,n}\left(a_{i,mn}e^{i\gamma_{mn}z} + a_{r,mn}e^{-i\gamma_{mn}z}\right)\Psi_{mn}(r,\theta), \tag{2}$$

where $a_{i,mn}$, $a_{r,mn}$ denote the amplitude of $(m,n)^{\text{th}}$ (where $m = 0, 1, 2\ldots M\text{-}1$; $n = 0, 1, 2\ldots N\text{-}1$) mode of the incident and reflected wave, respectively, $\Psi_{mn}(r,\theta)$ is the mode shape function of the cross-section of the pipe, k_{mn} is the modal wavenumber which can be obtained from the zero velocities boundary condition imposed on a rigid wall of the pipe [18] yielding:

$$J'_{\text{m}}(k_{mn}r)|_{r=R} = 0 \tag{3}$$

where $J_m(\cdot)$ is the m^{th} order of Bessel function of the first kind. In Eq. (3) $'$ denotes partial derivative with respect to r with $J'_{\text{m}}(x) = J_{m-1}(x) - \frac{m}{x}J_m(x)$. Note that an assumption of an air-filled pipe with rigid (zero normal particle velocity at the wall surface) and smooth wall is used here [19,20]. The assumption of rigid walls is justified by almost 4 orders of magnitude mismatch between the characteristic acoustic impedances of air 1.29 kg/m^3 × 343 m/s, and a uPVC pipe 1330 kg/m^3 × 2400 m/s. It is also noted that in Eq. (2)

z-axis wavenumber γ_{mn} is given by [18]:

$$\gamma_{mn} = \sqrt{k_0^2 - k_{mn}^2}. \tag{4}$$

Eq. (4) predicts the wavenumber for different modes at different frequencies, which means that the phase velocity is frequency and mode number dependent. When the free field wavenumber k_0 greater than the modal wavenumber k_{mn}, or the frequency is above the corresponding eigenfrequency f_{mn}, the (m,n) acoustic mode can propagate along the pipe. Otherwise, this mode is evanescent. This phenomenon is usually characterised with a dispersion relationship between the wavenumber γ_{mn} and frequency f. In this work, the dimensionless frequency kR will be used to generalise the proposed method for any pipe diameter.

The acoustic pressure in semi-infinite domain D_3 (see Fig. 1) is defined by the outgoing acoustic waves only yielding:

$$p_3 = \frac{1}{\sqrt{2\pi}} \sum_{m,n} c_{t,mn} e^{\mathrm{i}\gamma_{mn}(z-L)} \Psi_{mn}(r,\theta), \tag{5}$$

where $c_{t,mn}$ denotes the amplitude of the transmission sound.

In the domain D_2 (see Fig. 1) the pressure field in the blockage area is assumed to be represented by *closed* cavity modes [11–14], which can be written as:

$$p_2 = \sum_{\mu,l} b_{\mu l} \Phi_{\mu l}(r,\theta,z), \tag{6}$$

where $b_{\mu l}$ denotes the amplitude of each mode shape function of $\Phi_{\mu l}(r,\theta,z)$. The mode shape function $\Phi_{\mu l}(r,\theta,z)$ in the domain D_2 satisfies:

$$\left(\nabla^2 + k_{\mu l}^2\right)\Phi_{\mu l}(r,\theta,z) = 0. \tag{7}$$

In the above equation $k_{\mu l}$ is the eigenvalue of the domain D_2 (i.e. cavity) given by:

$$k_{\mu l}^2 = k_\mu^2 + \left(\frac{l\pi}{L}\right)^2, \tag{8}$$

where k_μ is the eigenvalue of the cross-section mode $\mu = (\hat{m},\hat{n})$ in domain D_2, $\hat{m}$=0, 1, 2…$\widehat{M}$-1; $\hat{n}$=0, 1, 2…$\widehat{N}$-1. Due to the assumption of Neumann boundary condition for which $\partial\Phi_{\mu l}/\partial\mathbf{n}$ on the walls of the closed cavity, $\Phi_{\mu l}(x,y,z)$ can be expressed as:

$$\Phi_{\mu l}(r,\theta,z) = \left[\frac{1}{\phi}\varphi_\mu(r,\theta)\right]\left[\sqrt{\frac{2-\delta_{l0}}{L}}\cos\left(\frac{l\pi}{L}z\right)\right], \tag{9}$$

where $l = 0, 1, 2, 3\ldots L_N$-1, $\varphi_\mu(r,\theta)$ is the mode shape of the cross-section of domain D_2, and ϕ is the normalisation factor calculated from the inner product of mode shape $\varphi_\mu(r,\theta)$:

$$\phi = \sqrt{\iint_{S_i} \varphi_\mu(r,\theta)\varphi_\mu{}^*(r,\theta) r \mathrm{d}r\mathrm{d}\theta}, \ \textit{where } i = 1,2 \tag{10}$$

within which superscript $\varphi_\mu{}^*$ refers to complex conjugate of φ_μ, δ_{l0} is the Dirac function which equals to 1 when $l = 0$, and equals to 0 when $l \neq 0$. The integral area S_1 and S_2 is the interface area between the waveguide domains (D_1 and D_3) and the blockage/robot cavity (domain D_2) (see Fig. 1).

Multiplying Eq. (7) by p and subtracting Eq. (1) multiplied by $\Phi_{\mu l}$ gives [18]:

$$\iiint_V \left[p\nabla^2\Phi_{\mu l} - \Phi_{\mu l}\nabla^2 p + \left(k_{\mu l}^2 - k_0^2\right)\Phi_{\mu l} p\right]\mathrm{d}V = \mathrm{i}\rho_0\omega Q_S(\omega)\Phi_{\mu l}(\mathbf{r}_s) \tag{11}$$

where the integral volume V is the volume of blockage/robot cavity in domain D_2. Using the Green's theorem Eq. (11) can be simplified to:

$$\iint_{S_1 S_2} \left(p\nabla\Phi_{\mu l} - \Phi_{\mu l}\nabla p\right)\cdot\mathbf{n}\mathrm{d}S + \iiint_V \left(k_{\mu l}^2 - k_0^2\right)\Phi_{\mu l} p \mathrm{d}V = \mathrm{i}\rho_0\omega Q_S(\omega)\Phi_{\mu l}(\mathbf{r}_s) \tag{12}$$

where $\mathbf{n}$ is the normal to the coupling surface.

The closed cavity mode in Eq. (6) satisfies $\nabla\Phi_{\mu l}\cdot\mathbf{n} = 0$ at the coupling surfaces S_1 and S_2. Substituting Eqs. (2)–(6) into Eq. (12) and applying the orthogonality of the modes $\Phi_{\mu l}$ gives:

$$\sum_{mn}\left[\mathrm{i}\gamma_{mn}a_{i,mn}-\mathrm{i}\gamma_{mn}a_{r,mn}-\mathrm{i}\gamma_{mn}c_{t,mn}\cos(l\pi)\right]\chi_{\mu,mn}+\left(k_{\mu l}^2-k_0^2\right)b_{\mu l}=\mathrm{i}\rho_0\omega Q_S(\omega)\Phi_{\mu l}(\mathbf{r}_s), \tag{13}$$

with

$$\chi_{\mu,mn}=\iint_S\frac{1}{\phi}\varphi_\mu(r,\theta)\Psi_{mn}(r,\theta)\mathrm{d}S,\ S=S_1\ \text{or}\ S_2. \tag{14}$$

The above integral is evaluated over S_1 or S_2 to account for the coupling between the waveguide and the cavity. Based on the orthogonality of the modes $\Psi_{mn}(r,\theta)$, the continuity condition for the sound pressure at the interfaces is:

$$a_{i,mn}+a_{r,mn}=\sum_{\mu,l}b_{\mu l}\chi_{\mu,mn},\ \text{for}\ S_1, \tag{15}$$

$$c_{t,mn}=\sum_{\mu,l}b_{\mu l}\cos(l\pi)\chi_{\mu,mn},\ \text{for}\ S_2. \tag{16}$$

Substitution of Eqs. (15) and (16) into Eq. (13) leads to the following system of equations:

$$\left(\mathbf{H}-k_0^2\mathbf{I}\right)\mathbf{b}=-2\mathrm{i}\boldsymbol{\chi}\mathrm{diag}[\boldsymbol{\gamma}]\mathbf{a}_i+\mathrm{i}\rho_0\omega Q_S(\omega)\boldsymbol{\Phi}(\mathbf{r}_s), \tag{17}$$

where $\mathbf{I}$ is a $(\widehat{M}\widehat{N}L_N\times\widehat{M}\widehat{N}L_N)$ identity matrix, diag[] transfers a vector into a diagonal matrix where the diagonal elements are composed of the vector, and other non-diagonal elements are zeros. diag[$\boldsymbol{\gamma}$] is a $(MN\times MN)$ diagonal matrix with its diagonal elements defined by $\gamma_{mn}=\sqrt{k_0^2-k_{mn}^2}$. $\mathbf{b}$ is a $(\widehat{M}\widehat{N}L_N\times 1)$ vector that expresses the amplitude of the modal response in the domain D_2. $\mathbf{a}_i$ is a $(MN\times 1)$ vector which expresses the amplitude of the modal response of the incident wave. $\boldsymbol{\chi}$ is a $(\widehat{M}\widehat{N}L_N\times MN)$ matrix that expresses the coupling between the waveguide and the cavity with its elements defined in Eq. (14). $\boldsymbol{\Phi}(\mathbf{r}_s)$ is a vector $(\widehat{M}\widehat{N}L_N\times 1)$ that denotes the modal excitation components. $\mathbf{H}$ is $(\widehat{M}\widehat{N}L_N\times\widehat{M}\widehat{N}L_N)$ matrix (also referred to as the effective non-Hermitian Hamiltonian matrix in [13,14,21]) given by:

$$\mathbf{H}=\mathrm{diag}\left[k_{\mu l}^2\right]-\mathrm{i}\boldsymbol{\chi}\mathrm{diag}[\boldsymbol{\gamma}]\boldsymbol{\chi}^T-\mathrm{i}\mathrm{diag}\left[(-1)^l\right]\boldsymbol{\chi}\mathrm{diag}[\boldsymbol{\gamma}]\boldsymbol{\chi}^T\mathrm{diag}\left[(-1)^l\right], \tag{18}$$

within which the symbol Tdenotes conjugate transpose. $\mathrm{diag}\left[(-1)^l\right]$ is a $(\widehat{M}\widehat{N}L_N\times\widehat{M}\widehat{N}L_N)$ diagonal matrix with the elements on the main diagonal defined by $(-1)^l$. It is noted that the first term of the matrix $\mathbf{H}$ in Eq. (18) contains the eigenvalues of the rigid cavity defined by Eq. (8) in the absence of coupling with the waveguide domains D_1 and D_3, whereas the second and third terms describe the coupling between the cavity, domains D_1 and D_3, respectively. The last two terms in Eq. (18) contain the wavenumbers for all the modes including the evanescent modes. These modes are important to account for because of the complexity of the acoustic scattering effect at the cross-sectional change in the pipe.

2.2. Trapped modes

The matrix $\mathbf{H}$ can be used to formulate the eigenvalue problem to analyse the trapped modes in the domain D_2:

$$\mathbf{H}\mathbf{V}_{\mu l}=K_{\mu l}^2\mathbf{V}_{\mu l}, \tag{19}$$

where $K_{\mu l}^2$ denotes the frequency dependent eigenvalues of the matrix $\mathbf{H}$, and $\mathbf{V}_{\mu l}$ denotes the associated eigenvectors. Note that here $K_{\mu l}^2$ is different from $k_{\mu l}^2$ in Eq. (18) because the eigen-value $\left(K_{\mu l}^2\right)$ of the matrix $\mathbf{H}$ contains information about the coupling between the cavity and the waveguide, whereas $k_{\mu l}^2$ is the eigenvalue of the *closed* rigid cavity. Since $\mathbf{H}$ is a symmetric matrix, its eigenvectors are bi-orthogonal [22]. Therefore, the response amplitude in the domain D_2 using Eq. (17) can be rewritten as:

$$\begin{aligned}\mathbf{b}&=\left(\mathbf{H}-k_0^2\mathbf{I}\right)^{-1}[-2\mathrm{i}\boldsymbol{\chi}\mathrm{diag}[\boldsymbol{\gamma}]\mathbf{a}_i+\mathrm{i}\rho_0\omega Q_S(\omega)\boldsymbol{\Phi}(\mathbf{r}_s)]=\mathbf{V}\left(\mathbf{V}\mathbf{H}\mathbf{V}^{-1}-k_0^2\mathbf{V}\mathbf{V}^{-1}\right)^{-1}\mathbf{V}^T[-2\mathrm{i}\boldsymbol{\chi}\mathrm{diag}[\boldsymbol{\gamma}]\mathbf{a}_i+\mathrm{i}\rho_0\omega Q_S(\omega)\boldsymbol{\Phi}(\mathbf{r}_s)]\\&=\mathbf{V}\left(\mathbf{K}^2-k_0^2\mathbf{I}\right)^{-1}\mathbf{V}^T[-2\mathrm{i}\boldsymbol{\chi}\mathrm{diag}[\boldsymbol{\gamma}]\mathbf{a}_i+\mathrm{i}\rho_0\omega Q_S(\omega)\boldsymbol{\Phi}(\mathbf{r}_s)],\end{aligned} \tag{20}$$

where $\mathbf{K}$ is a $(\widehat{M}\widehat{N}L_N\times\widehat{M}\widehat{N}L_N)$ diagonal matrix with its elements $K_{\mu l}$ determined with Eq. (19), $\mathbf{V}$ is the matrix that contains the eigenvectors $\mathbf{V}_{\mu l}$ (see Eq. (19)). The singular points of the acoustic response are at:

$$\mathrm{Re}\{K_{\mu l}(\omega)\}=k_0 \tag{21}$$

when $\mathrm{Im}\{K_{\mu l}(\omega)\}=0$. Therefore, $K_{\mu l}(\omega)$ are the complex resonance frequencies which can also be used to estimate the trapped modes eigenfrequencies in domain D_2.

2.2.1. Response corresponding to point source excitation

In this section, we only consider scattering caused by an artefact in the presence of acoustic source positioned in the domain D_2. It is noted that the point source is considered in the absence of any incident wave in the domain D_1 so that the first term in the right-hand side of Eq. (17) corresponding to the incident wave can be ignored. The acoustic response at any arbitrary receiver point, $\mathbf{r}_r$, in domain D_2 can be expressed as:

$$p_2(\omega,\mathbf{r}_r)=\sum_{\mu,l}b_{\mu l}\Phi_{\mu l}(\mathbf{r}_r)=\mathrm{i}\rho_0\omega Q_S(\omega)\boldsymbol{\Phi}(\mathbf{r}_r)^T\left(\mathbf{H}-k_0^2\mathbf{I}\right)^{-1}\boldsymbol{\Phi}(\mathbf{r}_s). \tag{22}$$

If the receiver is outside the cavity, i.e. anywhere in the domain D_3, the response can be obtained by combining Eqs. (5), (16) and (17):

$$p_3(\omega,\mathbf{r}_r)=\frac{\mathrm{i}\rho_0\omega Q_S(\omega)}{\sqrt{2\pi}}\boldsymbol{\Psi}(\mathbf{r}_r)^T\left[e^{\mathrm{i}\gamma(z_r-L)}\right]\boldsymbol{\chi}^T\mathrm{diag}\left[(-1)^l\right]\left(\mathbf{H}-k_0^2\mathbf{I}\right)^{-1}\boldsymbol{\Phi}(\mathbf{r}_s). \tag{23}$$

Similarly, the response at a receiver point in the domain D_1 can be written as:

$$p_1(\omega,\mathbf{r}_r)=\frac{\mathrm{i}\rho_0\omega Q_S(\omega)}{\sqrt{2\pi}}\boldsymbol{\Psi}(\mathbf{r}_r)^T\left[e^{\mathrm{i}\gamma\ (L-z_r)}\right]\boldsymbol{\chi}^T\left(\mathbf{H}-k_0^2\mathbf{I}\right)^{-1}\boldsymbol{\Phi}(\mathbf{r}_s). \tag{24}$$

2.3. Incident wave and scattering matrix estimation

In this section we discuss the scattering of the incident wave caused by a blockage. Therefore, the term associated with the point source located in the domain D_2 can be ignored. Substituting Eq. (17) into Eq. (15) gives the reflection coefficient $r_{m_2n_2,m_1n_1}$ for the incident mode (m_1, n_1) with the amplitude a_{i,m_1n_1} reflected into the mode (m_2, n_2) with the amplitude a_{r,m_2n_2}:

$$r_{m_2n_2,m_1n_1}=\frac{a_{r,m_2n_2}}{a_{i,m_1n_1}}=-\delta_{m_2m_1}\delta_{n_2n_1}-2\mathrm{i}\chi_{m_2n_2}\left(\mathbf{H}-k_0^2\mathbf{I}\right)^{-1}\gamma_{m_1n_1}\chi_{m_1n_1}. \tag{25}$$

The transmission coefficient $t_{m_2n_2,m_1n_1}$ for the incidence mode (m_1, n_1) with the amplitude a_{i,m_1n_1} transmitted into the mode (m_2, n_2) with the amplitude c_{t,m_2n_2} is:

$$t_{m_2n_2,m_1n_1}=\frac{c_{t,m_2n_2}}{a_{i,m_1n_1}}=-2\mathrm{idiag}\left[(-1)^l\right]\chi_{m_2n_2}\left(\mathbf{H}-k_0^2\mathbf{I}\right)^{-1}\gamma_{m_1n_1}\chi_{m_1n_1}. \tag{26}$$

Eqs. (25) and (26) will be used to calculate the reflection and transmission coefficients associated with mode conversion caused by the blockage.

2.4. Mode shapes in the waveguides and cavity

The mode shape function $\Psi_{mn}(r,\theta)$ in Eqs. (2) and (5) can be written as:

$$\Psi_{mn}(r,\theta)=\begin{cases}\dfrac{1}{\sqrt{\pi}RJ_0(k_{0n})}J_0(k_{0n}r),\ m=0,\\ \sqrt{\dfrac{1}{k_{mn}^2-m^2}}\ \dfrac{k_{mn}}{\sqrt{\pi}RJ_m(k_{mn})}\exp(\mathrm{i}m\theta)J_m(k_{mn}r),\ m\neq 0.\end{cases} \tag{27}$$

For a 3D axisymmetric blockage or robot body (as shown in Fig. 1a), the mode shape function of the annular pipe (see Eq. (9)) can be simplified as [23]:

$$\varphi_\mu(r,\theta)=\beta_{\hat{m}\hat{n}}\left[Y_{\hat{m}}'\left(\frac{1}{2}\eta_{\hat{m}\hat{n}}h\right)J_{\hat{m}}(\eta_{\hat{m}\hat{n}}r)-J_{\hat{m}}'\left(\frac{1}{2}\eta_{\hat{m}\hat{n}}h\right)Y_{\hat{m}}(\eta_{\hat{m}\hat{n}}r)\right]\exp(\mathrm{i}\hat{m}\theta), \tag{28}$$

where

$$\beta_{\hat{m}\hat{n}}=\frac{\eta_{\hat{m}\hat{n}}}{\sqrt{2}}\Bigg/\sqrt{\left(\frac{J_{\hat{m}}'\left(\frac{1}{2}\eta_{\hat{m}\hat{n}}h\right)}{J_{\hat{m}}'(\eta_{\hat{m}\hat{n}}R)}\right)^2\left(1-\frac{\hat{m}^2}{\eta_{\hat{m}\hat{n}}^2R^2}\right)-1+\frac{\hat{m}^2}{\eta_{\hat{m}\hat{n}}^2R^2}}, \tag{29}$$

and $\frac{1}{2}\eta_{\hat{m}\hat{n}}h$ is the $(\hat{n}+1)^{\text{th}}$ positive root of the transcendental equation $Y_{\hat{m}}'(x)J_{\hat{m}}\left(\frac{1}{2}xh/R\right)-J_{\hat{m}}'(x)Y\left(\frac{1}{2}xh/R\right)=0$, and $Y_{\hat{m}}(\cdot)$ is the $\hat{m}^{\text{th}}$ Bessel function of the second kind.

For a small moon-shape blockage ($h/R<1$) (see Fig. 1(c) and (d)), the non-axisymmetric modes split into two modes whereas the axisymmetric modes do not split but the eigenvalues are slightly shifted [24]. An example of the mode split phenomenon of the first

non-axisymmetric mode is shown in Fig. 2 adapted from [24]. $\varphi_\mu(r,\theta)$ can be obtained analytically [24] or numerically from the modal analysis.

3. Results and discussion

This section compares the predictions obtained with the analytical and numerical models for acoustic waves scattered by a blockage. A cylindrical pipe with rigid walls and a diameter of 150 mm was considered. The trapped modes analysis and point source excitation analysis were implemented using FEM in Comsol Multiphysics 6.0 with Perfectly Matched Layer (PML) at both ends of the pipe. The mesh elements were smaller than a 1/10-th of the minimum acoustic wavelength. The origin of the measured data is explained in the previous publication [5]. These data are also presented here for the experimental validation of the proposed analytical model used to predict the reflection coefficient. The analytical model used 20 modes in the pipe (modes index (m, n) in the domains D_1 and D_3), 20 cross-sectional (modes with index $\mu = (\hat{m},\hat{n})$) and 40 axial (modes index l) modes in the cavity (domain D_2).

3.1. Axisymmetric model

3.1.1. Trapped modes

This section discusses the trapped modes predicted with the theoretical model detailed in Section 2. For a cylindrical empty pipe, the eigen-frequencies of the first three modes (apart from the fundamental mode) can be estimated from Eq. (3). These are shown with solid vertical green lines in Fig. 3 at $k_{10}R$=1.841, $k_{20}R$ =3.054, $k_{01}R$ =3.832, respectively. A cylindrical blockage with 1.2R in diameter, and L = 2R in length was located at the centre of the cross section. This choice for the diameter of the axisymmetric body for the subsequent simulation is relatively large and somewhat extreme. It was chosen to demonstrate the ability of the proposed model to cope with a complexity of the acoustic scattering problem when the body size is comparable to the pipe's diameter. The first two eigenfrequencies of the annual pipe (domain D_2), that can be predicted using the transcendental equation (Eq. (28)), are at kR=1.26 for mode (1,0) and at kR=2.51 for mode (2,0) (shown in Fig. 3(a) with the vertical green dashed lines).

The cut-off frequency of the first non-axisymmetric mode (1,0) in the domain D_2 (annular pipe) is observed at kR=1.26 which is smaller than the cut-off frequency of the same mode in the empty pipe in domains D_1 and D_3 (kR =1.84). Intuitively, the first non-axisymmetric wave pattern in the frequency range kR from 1.26 to 1.84 (grey regime in Fig. 3(a)) can propagate in the annular pipe (domain D_2) but not in the domains D_1 and D_3. Therefore, this mode is expected to be restricted (or so-called trapped) within the domain D_2. This trapped wave physics was analyzed using the eigenvalue decomposition of the symmetric matrix **H** as discussed in Section 2. It is shown in Fig. 3(a) that the frequency of the trapped eigenmode can be found as an intersection of the solution of Eq. (21) (the black solid line in Fig. 3a) with the eigenvalues of Eq. (19). For example, the trapped eigenmodes corresponding to the first two eigenvalues K_{100} and K_{101} of Eq. (19) highlighted in Fig. 3(a) as the black star points are observed at kR =1.39 and kR =1.69, where the solutions of Eq. (19) cross the solution of Eq. (21). These analytically predicted eigen-frequencies match with the numerical solution given in Ref. [9]. The shapes of trapped modes with index (1,0,0) and (1,0,1) at kR =1.39 and kR =1.69, respectively, are numerically calculated with Comsol as shown in Fig. 4. It is observed that the acoustic energy is concentrated in the annual pipe and decays rapidly in the unblocked parts of the pipe (domains D_1 and D_3) which means the wave does not propagate. This energy concentration may result in the acoustic reverberation with a long duration in the time domain if a broad band excitation is used for pipe inspection. It is likely to lead to issues with signal overlapping and to complicate faults detection or classification.

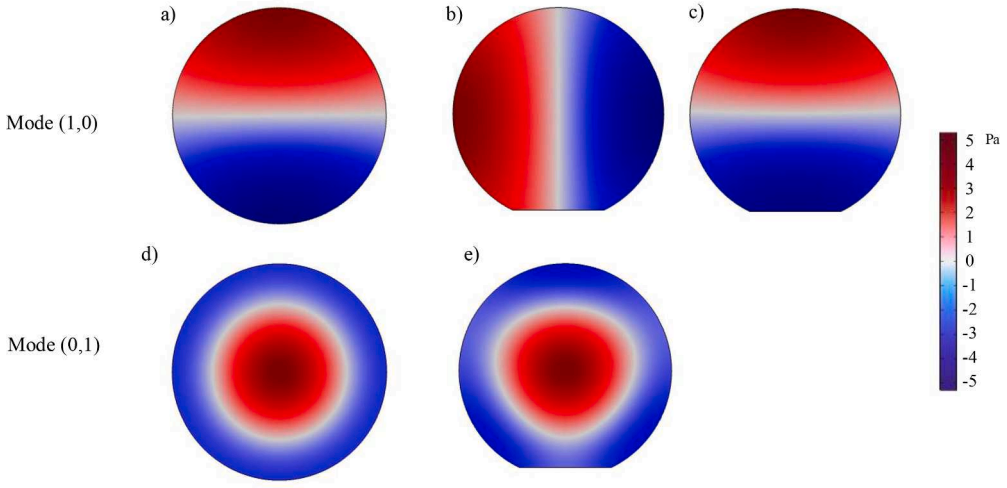

Fig. 2. An illustration of the mode shape changes caused by the presence of a moon-shape blockage. First row: (a) the original shape of non-axisymmetric mode (1,0); (b and c) splitting of the original mode into the anti-symmetric and symmetric modes, respectively. Second row: (d) the original shape of the axisymmetric mode (0,1); (e) the change in the axisymmetric mode shape caused by the blockage [24].

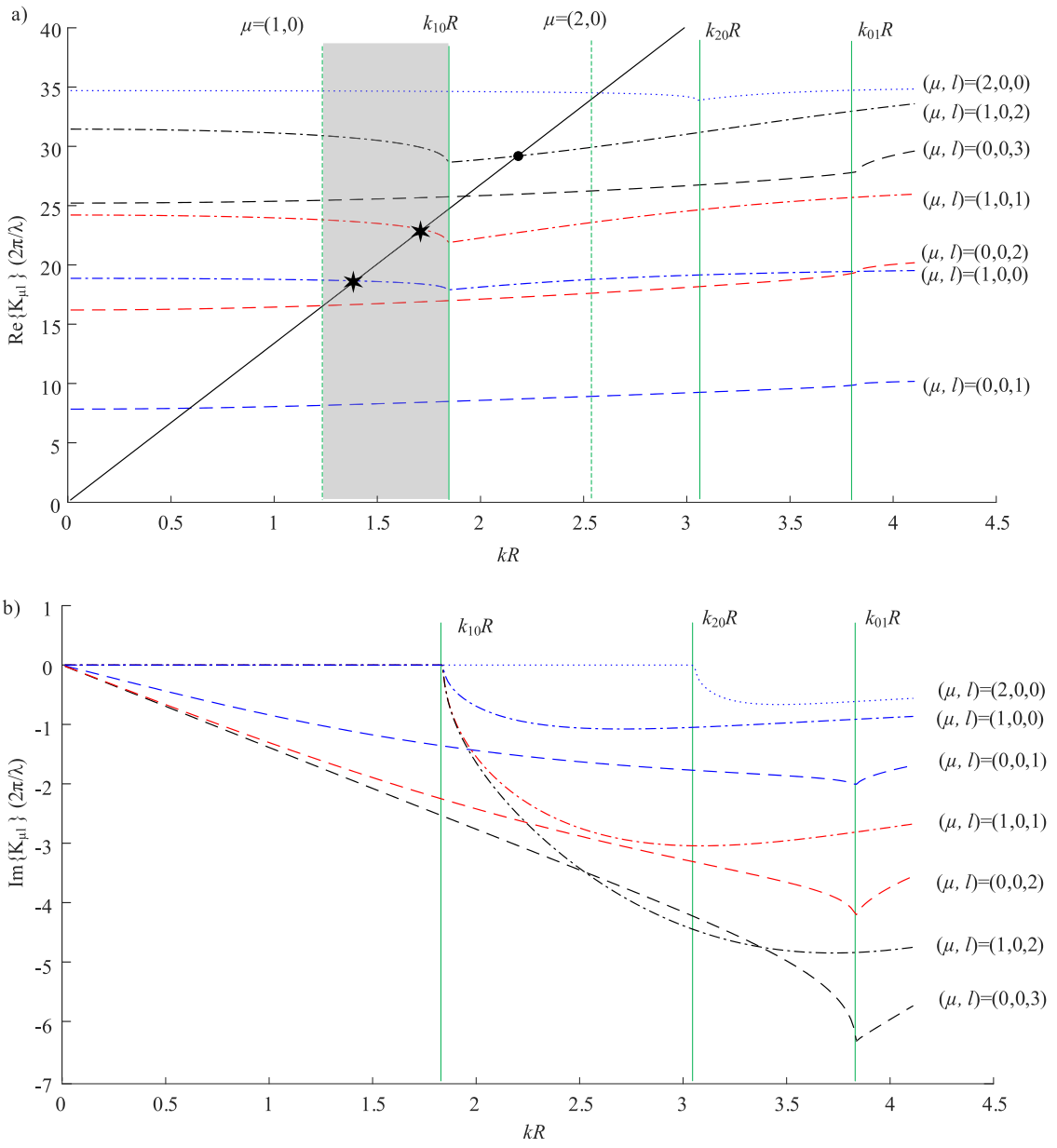

Fig. 3. (colour online). The frequency dependent eigenvalue $\boldsymbol{K}_{\mu l}$: (a) real part; (b) imaginary part with wavenumber $\boldsymbol{k}_0$(black solid line), $\boldsymbol{K}_{001}$ (blue dashed line), $\boldsymbol{K}_{002}$ (red dashed line), $\boldsymbol{K}_{003}$ (black dashed line), $\boldsymbol{K}_{100}$ (blue dash-dotted line), $\boldsymbol{K}_{101}$ (red dash-dotted line), $\boldsymbol{K}_{102}$ (black dash-dotted lines), $\boldsymbol{K}_{200}$ (blue dotted line), eigenfrequencies of the waveguide (green solid line), eigenfrequency of the annual pipe (green dashed lines). Two black star points are the first two eigenvalues $\boldsymbol{K}_{100}$ and $\boldsymbol{K}_{101}$ at kR =1.39 and kR =1.69. The black dot point is the eigenvalue of mode (1,0,2) at kR =2.20.

There exist extra two points satisfying $K_{\mu l} = k_0$ (Eq. (21)) below the first eigen-frequency (mode (1,0,0)) which corresponds to K_{001} and K_{002} eigenvalues of Eq. (19) (see Fig. 3(a)). This is due to the superposition of forwards and backwards propagating wave in the annual pipe caused by the discontinuity of the cross-section area in the plane wave regime. These modes have non-zero imaginary eigenvalues (see Fig. 3b) $\mathrm{Im}\{K_{\mu l}\} \neq 0$ which correspond to the case when acoustic energy can leak out from the cavity to the waveguide and propagate. Whereas the trapped modes (1,0,0) and (1,0,1) have zero imaginary part leading to the local energy concentration.

It is also observed that the amplitude of the real/imaginary eigenvalues of (0,0,1) and (0,0,2) axisymmetric modes increases almost linearly with frequency until it is close to the first axisymmetric mode (0, 1) of the pipe as shown in Fig. 3(a). On the other hand, the amplitude of the eigenvalues for the non-axisymmetric modes, e.g. μ=(1, 0) (see Fig. 3(a)) decreases with zero imaginary part until it is close to the corresponding non-axisymmetric mode.

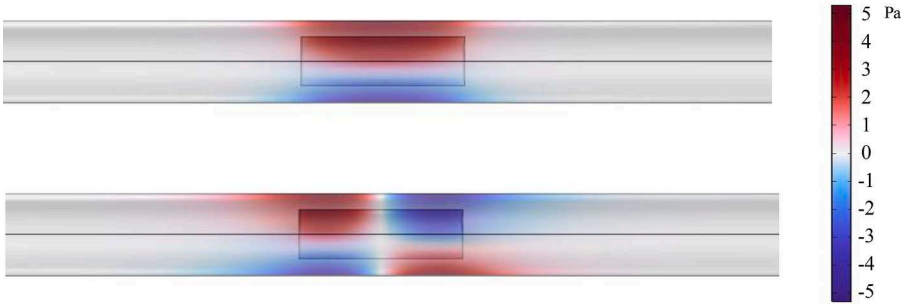

Fig. 4. (colour online). The trapped modes (1,0,0) at kR =1.39 (upper figure) and (1,0,1) at kR =1.69 (lower figure) from numerical simulation for the axisymmetric artefact with $L = 2R$ and $h = 1.2R$.

3.1.2. Point source excitation

This section analyses the acoustic response with point source excitation and single receiver close to the cylindrical rigid body in the pipe as shown in Fig. 5. In application to the acoustic inspection systems introduced in this paper this rigid body modelled a robotic platform where acoustic sensors are usually installed on the top of the robot for condition monitoring and defects detection in a sewage pipe to avoid a contact with the water flow at the bottom of the pipe. This type of installation of sensors is affected by the robot body due to the existence of a trapped mode in the adjacent air cavity.

For simplicity, in this paper the prediction of the trapped modes associated with the geometry illustrated in Fig. 5 was conducted for specific dimensions of the rigid body with $h = 1.2R, L = 2R$, fixed receiver location and two source positions. Fig. 6 shows the acoustic pressure predicted with the numerical and analytical models for a point source excitation (volume flow rate out from the source 0.001 m^3/s) being at the centre (in the middle of the top surface) of the cylindrical rigid body with the axial coordinate $z_s = 1/2L$ or off-centre at $z_s = 1/3L$. The receiver was fixed at $z_r = 2/3L$ (see Figs. 1 and 5 for notations). The radial coordinates of the excitation and the receiver were $r = h/2$ on the top of the body with $\theta = \pi$ (see Fig. 5). The blockage dimensions and its position were identical to that analysed for the trapped mode in Section 3.1.1 with the results shown in Fig. 3. It must also be noted that the receiver/source location was chosen to be off-centre and away from the nodal point of the trapped modes discussed in the Section 3.1.1. As shown in Fig. 6, the analytically predicted sound pressure and the FEM simulation agree withing 4 dB over the frequency range of kR<4 apart from the resonance frequencies. The resonances were predicted with the eigenvalues discussed in Section 3.1.1. When the eigenvalue has zero or relatively small imaginary part, the acoustic resonance is not damped leading to a sharp peak, e.g. the peaks at kR =1.39 and kR =1.69 in Fig. 6 corresponding to the eigenmodes (1,0,0) and (1,0,1) with zero imaginary components, respectively. On the contrary, mode (1,0,2) (black dot in Fig. 3(a)) with resonance around kR =2.20 presents smoother or wider peak which corresponds to the non-zero imaginary eigenvalue. Observed mode damping phenomenon can be understood as the acoustic energy leaking out from the cavity and acoustic wave propagating in both the cavity and waveguide. In the plane wave regime, the analytical model tends to overestimate the acoustic pressure (as seen in Figs. 6–8 below kR <0.6), which is due to some underestimation of the imaginary part of the eigenvalues introduced in Section 2.1. It is also noted that the discrepancy in the low frequency range observed in Figs. 6–8 makes in reality little impact on the accuracy of the analytical prediction because of the mid- to high-frequency range used in the robotic platform in a typical experiment. The size of the speaker deployed on a robot cannot be large making it difficult to excite acoustic waves below 500 Hz (which corresponds to kR=0.7 in a 150 mm diameter pipe). The placement of the source at the cylinder's middle point ($z_s = 1/2L$) precludes the excitation of the first axial modes of the annular pipe, i.e. mode (1,0,1), owing to the source's alignment with the nodal position.

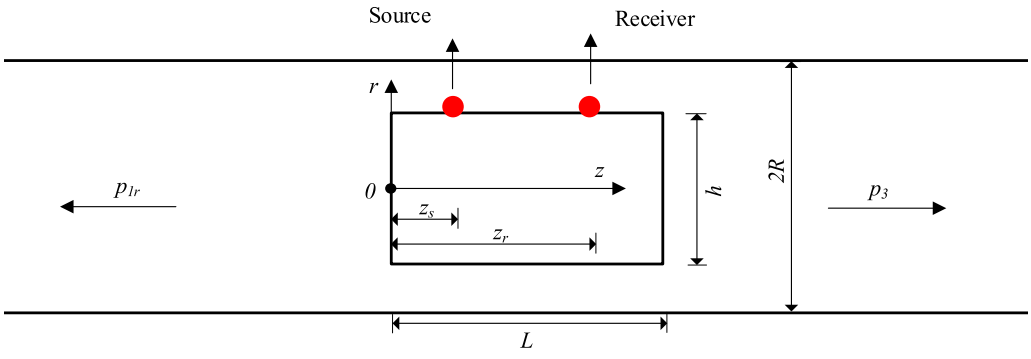

Fig. 5. An illustration of the geometry used for modelling of the acoustic response with a point source excitation on the robotic platform.

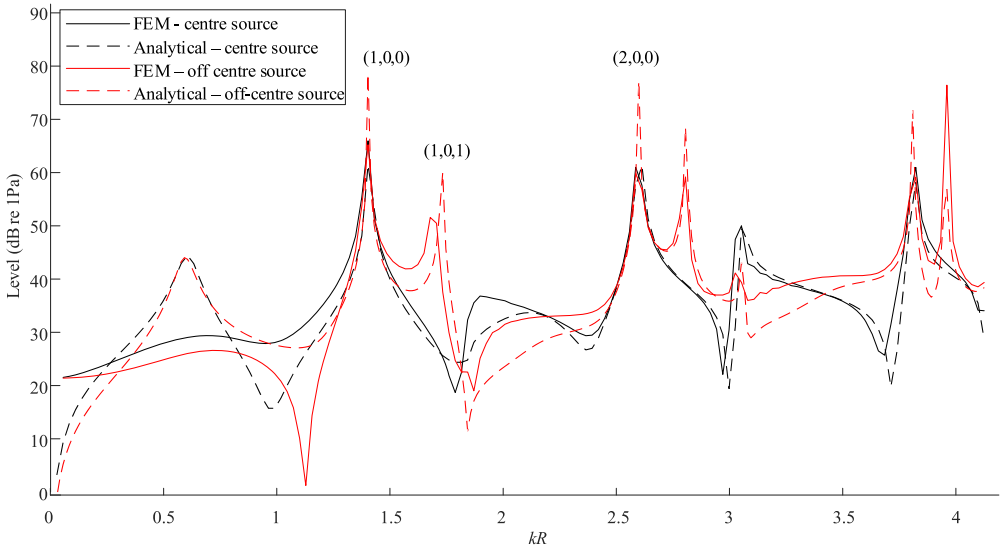

Fig. 6. A comparison of the acoustic frequency response predicted for a point source at the centre (black lines) $z_s = 1/2L$ or off-centre (red lines) $z_s = 1/3L$ of the cylinder surface in the pipe; $h = 1.2R$ (see also Fig. 5 for setup illustration).

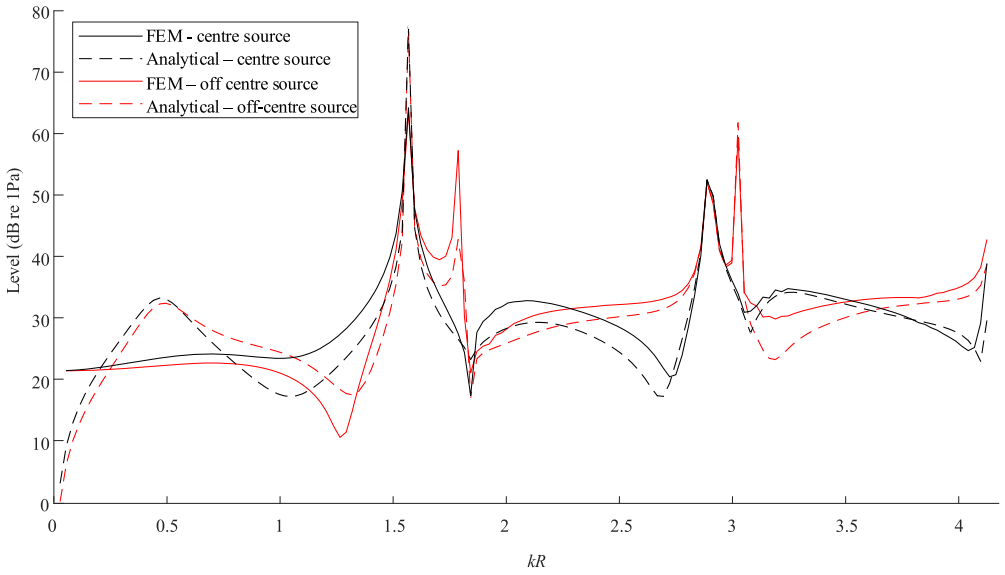

Fig. 7. A comparison of the acoustic response predicted for a point source at the centre (black lines) $\boldsymbol{z_s} = 1/2\boldsymbol{L}$, or off-centre (red lines) $z_s = 1/3L$ of the cylinder surface in the pipe; $h = 0.8R$ (see also Fig. 5 for setup illustration).

Fig. 7 and Fig. 8 show the acoustic response of a thinner cylindrical rigid body with $h = 0.8R$ and $h = 0.4R$, respectively. The agreement between the analytical model and FEM is closer when the cylinder is thinner. The averaged difference between analytical and FEM over the frequency range $0.7<kR<4.1$ for off-centre source and centre source is 3.2 dB and 2.4 dB, respectively, when $h = 0.8R$ (see Fig. 7), and 2.1 dB and 1.5 dB respectively when $h = 0.4R$ (see Fig. 8). For a thinner cylinder the number of undamped resonances is also reduced since the eigenfrequency of the annual pipe gets closer to the eigenfrequency of the empty pipe.

3.2. Non-axisymmetric model

3.2.1. Trapped mode

A half-moon blockage at the bottom of the pipe can split a non-axisymmetric mode into two modes (see Fig. 2): symmetric and anti-symmetric [24]. For a small blockage, this anti-symmetric mode has an eigenfrequency slightly lower than that of the first cut-off frequency ($k_{10}R$) of the empty pipe (see Fig. 4 from [24]) which then may result in a trapped mode in the frequency range

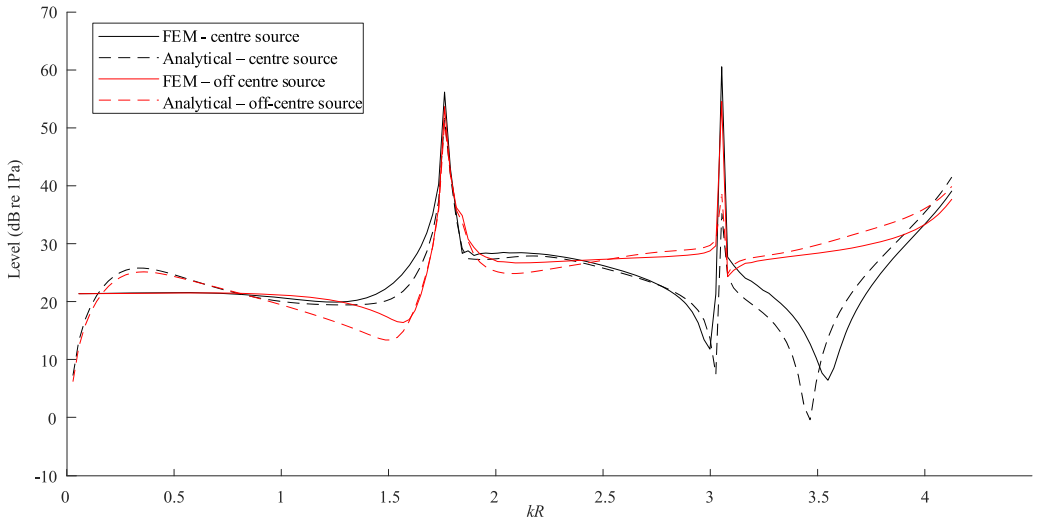

Fig. 8. A comparison of the acoustic frequency response predicted for a point source at the centre (black lines) $\boldsymbol{z_s} = 1/2\boldsymbol{L}$, or off-centre (red lines) $\boldsymbol{z_s} = 1/3\boldsymbol{L}$ of the cylinder surface in the pipe; $\boldsymbol{h} = 0.4\boldsymbol{R}$.

between the anti-symmetric mode and $k_{10}R$. The analytical model used the solution of the wavenumbers from Ref. [24] to obtain the mode shapes for both anti-symmetric and symmetric modes:

$$\boldsymbol{\varphi}_{\hat{m}n}^{(1)}(\boldsymbol{r},\boldsymbol{\theta}) = \sin(\widehat{\boldsymbol{m}}\boldsymbol{\theta})\boldsymbol{J}_{\hat{m}}\left(\boldsymbol{k}_{\hat{m}n}^{(1)}\boldsymbol{r}\right), \tag{30}$$

$$\boldsymbol{\varphi}_{\hat{m}n}^{(2)}(\boldsymbol{r},\boldsymbol{\theta}) = \cos(\widehat{\boldsymbol{m}}\boldsymbol{\theta})\boldsymbol{J}_{\hat{m}}\left(\boldsymbol{k}_{\hat{m}n}^{(2)}\boldsymbol{r}\right), \tag{31}$$

where $k_{\hat{m}n}^{(1)}$ and $k_{\hat{m}n}^{(2)}$ are determined empirically from Tables 1 and 2 in Ref. [24]. Note that this model is limited for blockages <20 % as proposed in Ref. [24].

As shown in Fig. 9 the first non-axisymmetric mode for an empty pipe has the eigenfrequency of kR=1.841, whereas for a 20 % blockage with the dimensions $h = 0.4R,\ L = 2R$, the first non-axisymmetric mode is split into an anti-symmetric and symmetric mode at kR=1.76 and kR=2.16, respectively. Between the anti-symmetric mode kR=1.76 and the first non-axisymmetric mode ($k_{10}R$), the trapped mode exists at around kR=1.81 (marked as star where the blue-dashed curve $Re\{K_{100}\}$ crosses with the black solid curve k_0 in Fig. 9(a)). In this case, the imaginary part of the eigenvalue $\mathrm{Im}\{K_{100}\}$ is close to zero as shown in Fig. 9(b). This analytical solution has close agreement with the numerical prediction at kR=1.83 with the mode shape shown in Fig. 10. In Fig. 10 the mode shape of the acoustic wave has an anti-symmetric mode pattern respected to the θ=0 plane (which is the nodal plane).

There also exist two extra points satisfying $Re\{K_{\mu l}\} = k_0$ below the first eigenfrequency $k_{10}R$: K_{001} and K_{002} (see Fig. 9). These roots are caused by the superposition of the forward and backward propagating modes in the annual pipe in the plane wave regime. Again, these modes have non-zero imaginary eigenvalues (see Fig. 9(b)) i.e., $\mathrm{Im}\{K_{\mu l}\} \neq 0$ which represent example of leaky modes.

3.2.2. Point source excitation

In this section, FEM and analytical model were used to estimate the acoustic response due to a point source excitation (volume flow rate out from the source 0.001 m^3/s) at an off-centre position: $\left(-h, \frac{L}{3}, \frac{L}{3}\right)$ in the presence of a 20 % blockage with $h = 0.4R,\ L = 2R$. With a point source at an off-centre position, almost all the modes can be excited. As shown in Fig. 11, there is a narrow peak at kR=1.83, which represents the anti-symmetric mode (1,0,0). This is due to the zero imaginary part of the eigenvalue of K_{100}. The other resonances tend to have wider peaks/troughs compared with mode $(1,0,0)$ over the frequency range up to kR=4. This matches with the mode analysis in the Section 3.2.1. The maximum difference between the analytical model and the FEM is less than 4.8 dB over the frequency range $0.1<kR<4$. The fluctuation observed in the analytical model, and the mismatch between the FEM and the analytical

Table 1
The mutual mean differences (Eq. (33)) between the reflection coefficient spectra predicted with the proposed analytical model, FEM simulation or measured in the experiment for the frequency range of kR<1.83 (10; 20; 30 % blockage ratio).

	$R_{r\alpha}$: Analytical	Numerical (FEM)	Measurement
$R_{r\beta}$: Analytical	—	1.7; 4.1; 9.6 %	10.2; 3.2; 6.5 %
Numerical (FEM)	1.8; 3.5; 7.9 %	—	10.3; 3.6; 4.4 %
Measurement	11.6; 3.1; 5.6 %	11.6; 4.2; 5.1 %	—

Table 2
The mutual mean differences (Eq. (33)) between the reflection coefficient spectra predicted with the proposed analytical model, FEM simulation or measured in the experiment for the frequency range of $kR>1.83$ (10 %; 20 %; 30 % blockage ratio).

	R_{ra} : Analytical	Numerical (FEM)	Measurement
R_{rfi}: Analytica zl	—	7.5; 19.4; 27.5 %	14.5; 29.9; 19.6 %
Numerical (FEM)	8.2; 18.2; 22.6 %	—	12.4; 34.5; 11.1 %
Measurement	16.6; 31.1; 19.2 %	14.6; 68.4; 18.6 %	—

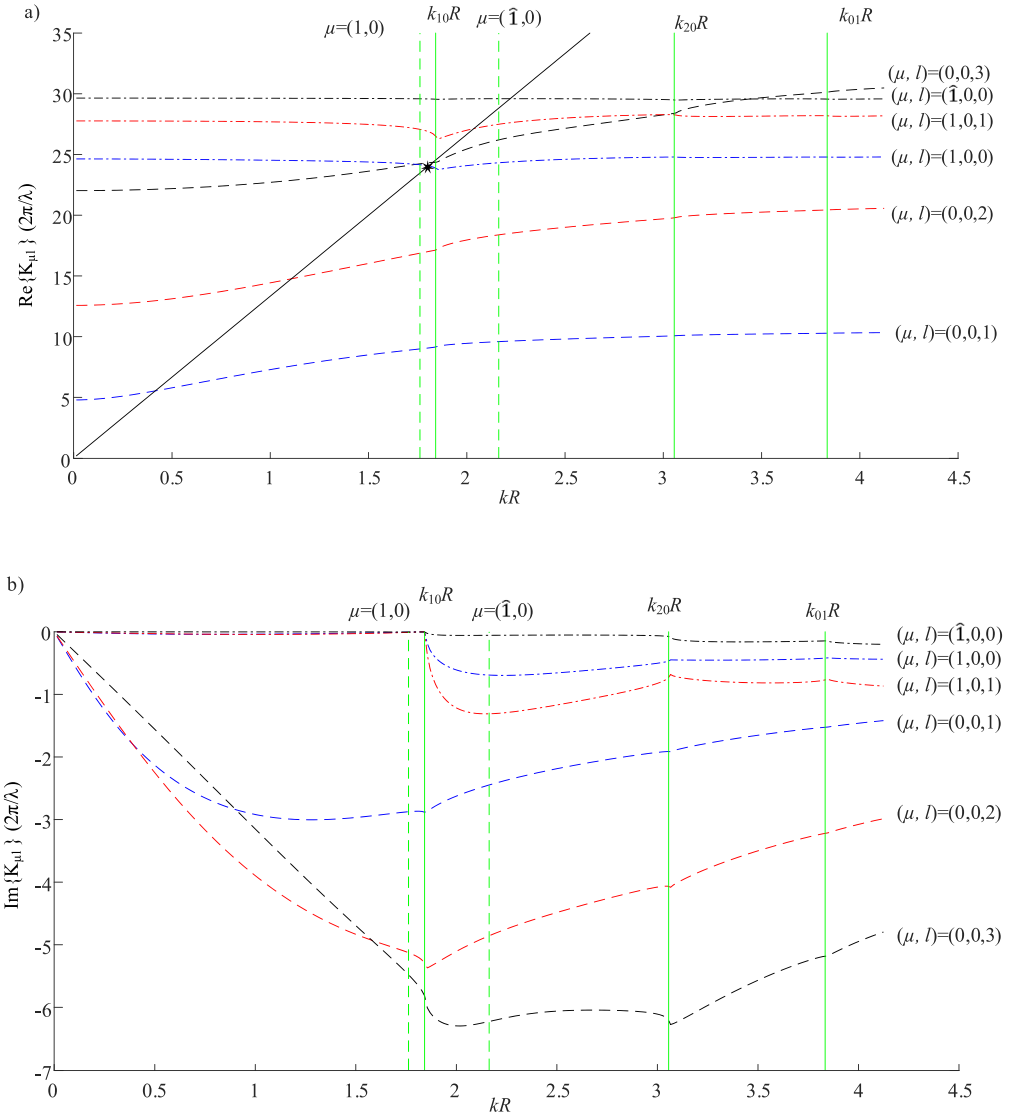

Fig. 9. The behaviour of the frequency dependent eigenvalue $K_{\mu l}$: (a) real part; (b) imaginary part for the pipe with a non-axisymmetric blockage ($h = 0.4R,\ L = 2R$) and wavenumber k_0 (black solid line), K_{001} (blue dashed line), K_{002} (red dashed line), K_{003} (black dashed line), K_{100} (blue dash-dotted line), K_{101} (red dash-dotted line), the symmetric mode $\widehat{K}_{100}$ mode (black dash-dotted line). The eigenfrequencies of the waveguide (green solid line), eigenfrequencies of the annual pipe (green dashed line).

models beyond the first cut-off frequency can be linked to inaccuracies in using the mode shapes (see Eqs. (30) and (31)) within the analytical model beyond the first cut-off frequency. This discrepancy is less than 3 dB within the frequency range of $kR<4$ for a blockage smaller than 20 % [24]. However, this error can be larger for blockages size over 20 %. For example, this maximum difference can be over 5 dB for a 30 % blockage.

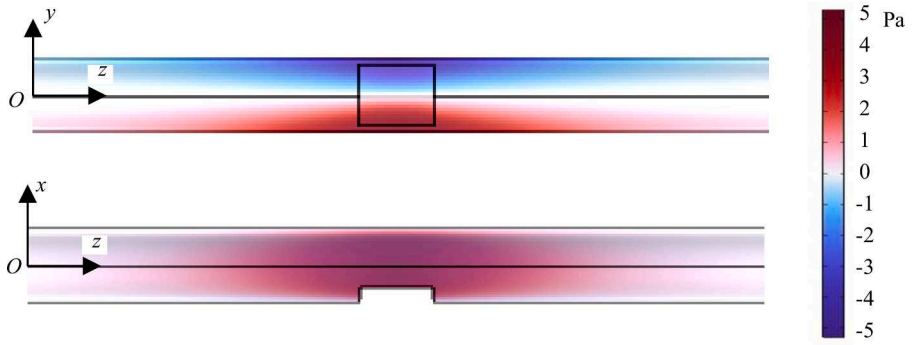

Fig. 10. The acoustics pressure of the trapped mode $(1, 0, 0)$ predicted with the numerical simulation for a 20 % non-axisymmetric blockage ($h = 0.4R$, $L = 2R$) located at the bottom of the pipe.

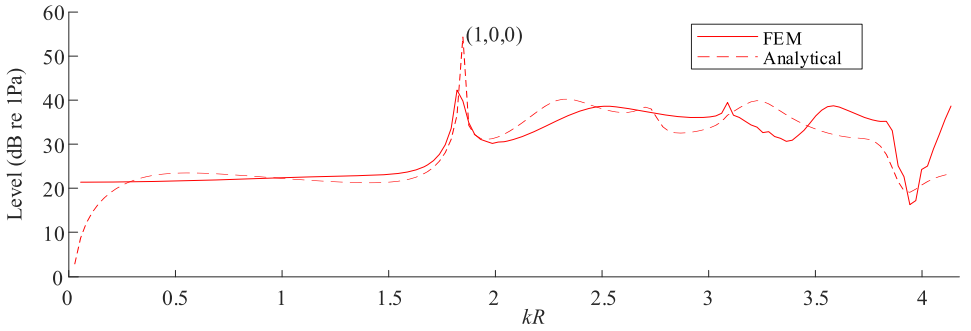

Fig. 11. A comparison of the acoustic frequency response predicted for a point source at the off-centre position, $\left(-\boldsymbol{h}, \frac{L}{3}, \frac{L}{3}\right)$ of the flat surface on the blockage; $\boldsymbol{h} = 0.4\boldsymbol{R}$.

3.3. *Experimental validation*

This section presents data on the acoustic reflection coefficient for a non-axisymmetric blockage in a typical drainage pipe. The data were obtained with a six-microphone array carried by a mobile testing platform (a remotely controlled robot (iRobot Looj 330 by iRobot [25]) similar to that detailed in [5,6]. This measurement setup is shown in Fig. 12. The measurements were carried out in the Integrated Civil and Infrastructure Research Centre (ICAIR) at Sheffield [26] to validate the analytical model proposed in Sections 3.1 and 3.2. A 16 m long straight section made of a few uPVC drainage pipes with the 150 mm diameter was used in this experiment (see Fig. 12(a)). Different sizes of concrete blockages ($\frac{h}{2R} = 0.1$, 0.2 and 0.3, i.e. 10 %, 20 % and 30 % blockages) were moulded and used to validate the analytical model and simulation. A photograph of these blockages is shown in Fig. 12(b). A complete termination ($\frac{h}{2R}$=1) was used as a reference blockage. The surface of the concrete blockages was assumed to be rigid, i.e. no more than 1 % of sound energy was absorbed in the adopted frequency range.

The acoustic sensor system consisted of a loudspeaker, six-microphone array, power amplifier for the speaker, 32-bit analogue to digital converter (ADC), digital to analogue converter (DAC) and Raspberry Pi 4 used for data acquisition and control as shown in Fig. 12(c). The sampling rate was set to 16 kHz. The microphone type used in this measurement was MSM321A3729H9CP by MEMSensing Microsystems Co. Ltd. Visaton 2242 speaker with the 32 mm diameter was driven with a 3 W power amplifier. Initially the speaker was located at the centre of the pipe within 5 mm positional error to minimise the excitation of non-axisymmetric modes. The microphone array was axisymmetrical with radius of 0.628R (see Fig. 12(c)) to follow the nodal line of the first axisymmetric mode (0, 1) for the empty pipe (see Fig. 2(e)). Therefore, the plane wave reflected from the blockage or other pipe features could be extracted and enhanced using an average of six microphones and wavelet denoising by sparse representation over the frequency range of $0.01<kR<4$.

A 100–3000 Hz ($0.01<kR<4.12$) sweep sine with 10 s duration was used as the excitation signal. The impulse response was obtained by deconvolution between the extracted plane wave and the excitation signal. The separation distance between the robot and the blockage was 5 m in the middle of the straight section of the pipe, so that the reflection pulse was time windowed for the calculation of the reflection coefficient. It is worth noting that the reflection coefficient from the 10 %, 20 % and 30 % blockages was normalised in the frequency domain by the reference signal measured for the reference 100 % blockage which was assumed as a rigid reflector with reflection coefficient equal to 1 across the adopted frequency range. The reflection coefficient was estimated from the acoustic impulse

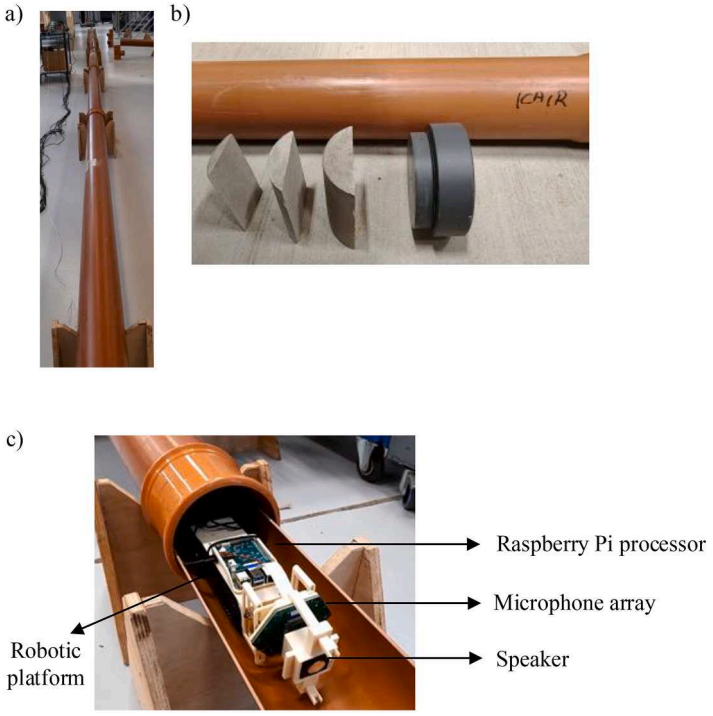

Fig. 12. (a) a straight pipe with 150 mm diameter and 16 m length; (b) concrete blockages with 10 %, 20 % and 30 % and 100 % (reference) blockage ratios ($\frac{h}{2R}\times$ 100%) as seen from left to right; (c) a robotic platform with microphone array and speaker.

response using the method detailed in [5]. Accordingly, it was predicted using the new analytical model detailed in Section 2.2 and FEM. The predictions were compared against the measured data. The reflection coefficient R_r can be defined as:

$$R_r(\omega) = p_r(\omega)/p_i(\omega) \tag{32}$$

where $p_i(\omega)$ is the spectrum of the incident sound wave measured using the sound reflection from a rigid termination, p_r is the spectrum of the sound wave reflected from the blockage.

Fig. 13 demonstrates a comparison between the measured reflection coefficient spectra, FEM simulation and analytical solution for the 10 %, 20 % and 30 % blockages. It is clear from Fig. 13 that the behaviour of the measured and simulated reflection coefficient spectra is different below the first cut-off frequency at $kR = 1.83$ and above it. The measured, simulated and analytically predicted spectra agree much better below $kR = 1.83$ but can deviate considerably above this frequency particularly for the blockage ratios greater than 10 %. Tables 1 and 2 present the mutual mean differences between the measured, simulated and analytically predicted reflection coefficient spectra estimated separately for the $kR < 1.83$ and $kR > 1.83$ frequency ranges as:

$$\epsilon_R = \frac{1}{W}\sum_{w=1}^{W}\frac{\left|R_{r\alpha}(\omega_w) - R_{r\beta}(\omega_w)\right|}{\max[R_{r\alpha}]}\times\ 100\%\ , \tag{33}$$

respectively. In the above equation $R_{r\alpha}$ is either the analytically predicted, simulated or measured reflection coefficient spectrum (columns in Tables 1 and 2) and $R_{r\beta}$ is the reference reflection coefficient spectrum against which this difference was estimated (rows in Tables 1 and 2). W in Eq. (33) is the total number of frequencies in the Fourier transform at which the difference was estimated.

In the $kR < 1.85$ frequency range the analytical model and FEM agree very well within $\epsilon_R \leq 4.1$ % for the small and medium blockages, i.e. 10 % and 20 % (See Table 1). In the case of the 30 % blockage the maximum difference increases to 9.6 %. With the increasing size of the blockage the frequency of the first minimum in the refection coefficient spectra (anti-resonance) decreases. This decrease is predicted with the analytical model, FEM simulation and confirmed with the measured data (see Fig. 13). For example, the trough for 10 % blockage is observed at around $kR = 1.44$, which is close to that for the 2D solution [18] (around $kR = 1.46$) with only the plane wave considered. For the 20 % blockage the anti-resonance is observed around $kR = 1.36$. This trough shifting phenomenon is caused by the coupling between the modes in the air cavity at the blockage location and the plane wave of the waveguide as explained in the previous sections. As the blockage becomes larger, e.g. 30 %, the analytical model overpredicts the frequency of the anti-resonance by 7.1 % (see Fig. 13). The frequency of this resonance predicted with the FEM simulation agrees with the measured data within 1.3 % for all the three blockage sizes.

When the blockage was 10 %, its reflection coefficient was also relatively small, i.e. well below $R_r(\omega) < 0.1$ (see Fig. 13). It is likely that the measured reflection coefficient for such a small blockage became comparable with the experimental errors expected with a 6-

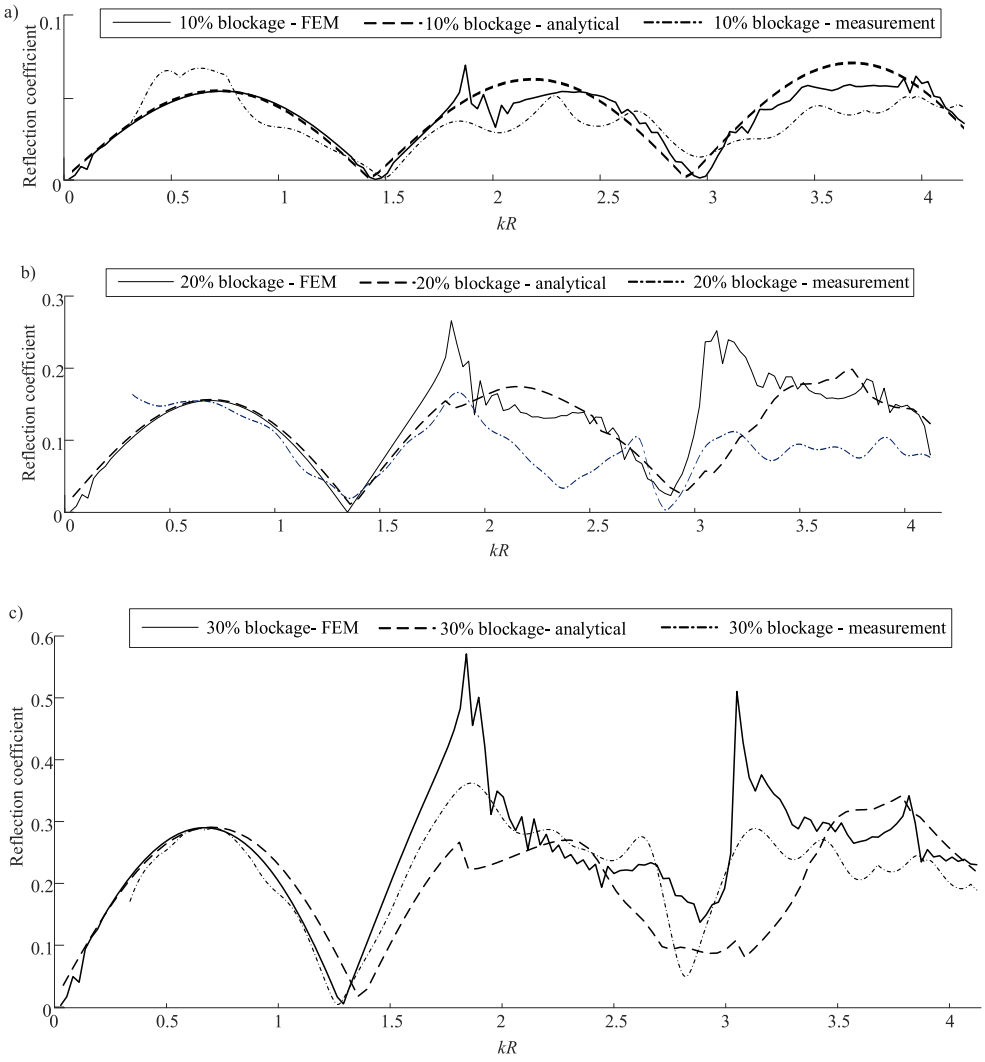

Fig. 13. A comparison of the reflection coefficient for: (a) 10 %, (b) 20 %, (c) 30 % blockages.

microphone cross-sectional array as explained in [5,6]. Also, the 32 mm diameter speaker used in the experiment struggled to ensure a sufficient signal-to-noise ratio below 500 Hz (i.e. below $kR \approx 0.7$ in Fig. 13). In the $kR < 1.85$ frequency range other factors such as poor pipe joints, wall vibration and scattering by the robot's body can also affect the quality of the measured data. In particular, the robot's body, speaker and array support shown in Fig. 12(c) are complicated in shape and the size of the whole arrangement is comparable to the acoustic wavelength. These factors are difficult to account for accurately in the FEM simulation and impossible with the proposed analytical model.

In the $kR > 1.85$ frequency range the behaviour of the reflection coefficient spectra predicted with the FEM for these three blockages becomes much more complex (see Fig. 13). Clear differences between the analytical model and FEM are visible in the results shown in Fig. 13, particularly for the 20 % and 30 % blockages. For these blockage ratios the maximum differences were 19.4 % and 27.5 % (see Table 2), respectively. In the vicinity of the cut-off frequencies the FEM simulation demonstrates clear resonance peaks that are not visible in the measured or analytically precited reflection coefficient spectra (see Fig. 13(b and c)). At these resonances the FEM simulated reflection coefficient is 50–100 % greater than the measured reflection coefficient. Key factors that affect the quality of the FEM simulation relate to scattering of sound by the robot's body, finite size of the speaker used in the experiment and the thermos-viscous effects in the pipe contributing to acoustic attenuation. These factors were neglected in the simulation. There are also clear differences between the analytical model and measured data (see Fig. 13). It was explained in Section 3.2.2 that the analytical model makes an assumption regarding the mode shapes and wavenumbers in Eqs. (30) and (31) used to calculate the acoustic pressure in the domain D_2 above the blockage (Fig. 1). This assumption breaks down beyond the first cut-off frequency when the blockage ratio increases above 20 % [24]. Therefore, it can be suggested that the proposed analytical model is more suitable for prediction of the acoustic reflection coefficient for smaller blockages, e.g. those with $h/(2R) \leq 0.2$. Proactive detection of these blockages is particularly important because they can be removed at a relatively low cost and when the probability of pollution and service disruption is low.

It is noted that the analytical model used in this paper is computationally much more efficient in calculating the reflection coefficient compared to the FEM simulation. The analytical model can be solved within 30 s for a blockage in a 150 mm diameter pipe with 20 Hz resolution over the frequency range 10–3000 Hz ($0.01<kR<4.12$) using Matlab Version 9.13 (R2022b) on a workstation with Intel(R) Core (TM) i7–9980 × 3.8 GHz CPU, and 128 GB RAM, whereas the computational time for the FEM model in Comsol executed on the same workstation is around 5 h (around 600 times slower).

4. Conclusions

A 3D analytical modal coupling method has been proposed to predict the acoustic wave scattering from an axisymmetric or non-axisymmetric artefact (i.e. blockage or robot's body) in a cylindrical waveguide such as a air-filled drainage pipe. The proposed method theoretically explains the existence of trapped modes due to the presence of a 3D axisymmetric or non-axisymmetric artefact in the pipe. These artefacts represent a robot's body or blockage that scatters the acoustic field in the pipe. The accuracy of the proposed analytical model has been estimated against a numerical simulation based on the final element method and validated against measured data. A comparison against the results of numerical simulation has demonstrated that the new analytical model is accurate withing 4 dB over the frequency range of $0.1<kR<4$ for an axisymmetric blockage with the blockage ratio of $h/(2R) = 0.6$. In the case of a non-axisymmertic blockage the difference between the proposed analytical model and numerical simulation has been within 3 dB for $h/(2R) < 0.2$. This difference can increase significantly for non-axisymmetric blockages with larger $h/(2R)$ ratios. However, the proposed analytical model is at least 600 times computationally more efficient that the FEM simulation.

The acoustic response of the pipe obtained with a point source excitation was predicted at six receiver points corresponding to the positions of microphones in an acoustic array installed in the pipe to detect and localise a non-axisymmetric blockage. The response has then been used to calculate the reflection coefficient for the 10 %, 20 % and 30 % blockages (i.e. 0.1, 0.2 and 0.3 blockage ratios). The analytical model demonstrates a 4.1 % agreement with the numerical and 11.5 % agreement with the measured reflection coefficient spectra in the frequency range below the first cut-off frequency $kR=1.83$. As the blockage becomes larger or the frequency range extends beyond $kR=1.83$ the difference between this analytical model and measured reflection coefficient data increases to 19.6 %. It has been observed that the frequency of the first anti-resonance in the reflection coefficient spectra shift towards the lower frequency range as the blockage ratio increases. This frequency shift caused by the coupling with the cavity modes and it has been predicted with the analytical model to within 2.7 % for the blockage ratios below 20 %.

There are several limitations of the proposed analytical model. Firstly, beyond the first cut-off frequency the classic mode shapes and wavenumbers assumed in Eqs. (30 and 31) are no longer accurate enough for blockage ratios above 20 % [24]. Secondly, the number of modes required for more precise calculations has to be much greater than that used in this work (20 modes in the pipe with index (m, n) in the domains D_1 and D_3, 20 cross-sectional modes with index $\mu = (\hat{m}, \hat{n})$ and 40 axial modes with index l in the domain D_2, see Section 2). Thirdly, it has been found difficult to validate accurately the new model against the FEM simulation or measured data. The FEM simulation used in this work has not included the exact robot shape that proved to be too sophisticated to be accurately modelled with the FEM. The FEM has not taken into account the finite size of the speaker used in the experiment and visco-thermal effects in the pipe. The reflection coefficient measured for the 10 % blockage has been found too low to measure it very accurately with a 6-microphone cross-sectional array for the reasons explained in [5,6]. Also, the 32 mm diameter speaker used in the experiment has not been powerful enough to ensure a sufficient signal-to-noise ratio below 500 Hz to validate the model below $kR=0.7$. Finally, other factors such as poor pipe joints, wall vibration and scattering by the complex robot's body shape could have also affected the quality of the measured data across the frequency range considered in this work. These factors are difficult to consider theoretically or with the FEM simulation adopted for this work. Our study suggests that the scattering pattern from a simple axisymmetric artefact in a pipe is very complex. The complexity of the scattering pattern increases progressively with the increased complexity of the artefact's shape. This topic deserves a separate systematic study through a more refined numerical simulation supported by a more extensive experimental work and machine learning.

CRediT authorship contribution statement

Yicheng Yu: Writing – review & editing, Writing – original draft, Visualization, Validation, Software, Methodology, Investigation, Formal analysis, Data curation. **Anton Krynkin:** Writing – review & editing, Writing – original draft, Supervision, Resources, Project administration, Methodology, Funding acquisition, Conceptualization. **Kirill V. Horoshenkov:** Writing – review & editing, Writing – original draft, Supervision, Resources, Project administration, Methodology, Funding acquisition, Conceptualization.

Declaration of competing interest

The authors declare that they have no known competing financial interests or personal relationships that could have appeared to influence the work reported in this paper.

Data availability

Data will be made available on request.

Acknowledgement

This work is supported by the UK Engineering and Physical Sciences Research Council (EPSRC) Programme Grant No. EP/S016813/1. ICAIR has been part funded by EPSRC, Grant UKCRIC-National Distributed Water Infrastructure Facility (EP/R010420/1) and the European Regional Development Fund (Project Number 28R15P00608) The authors would like to gratefully thank Mr. Gavin Sailor for kindly helping with the design of the robotic platform to support the acoustic sensing system. The authors would also like to gratefully thank Dr. Will Shepherd, Dr. Robin Mills and Mr. Paul Osbourne for kindly helping with the design of the blockages and providing other experimental facilities. For the purpose of open access, the authors have applied a 'Creative Commons Attribution (CC BY) licence to any Author Accepted Manuscript version arising.

References

[1] Discover Water. " Collecting & treating sewage," https://discoverwater.co.uk/treating-sewage (Accessed 21 March 2024).
[2] T.L. Nguyen, A. Blight, A. Pickering, G. Jackson-Mills, A.R. Barber, J.H. Boyle, R. Richardson, M. Dogar, N. Cohen, Autonomous control for miniaturized mobile robots in unknown pipe networks, Front. Robot. AI 9 (16) (2022).
[3] Y. Yu, A. Safari, X. Niu, B. Drinkwater, K.V. Horoshenkov, Acoustic and ultrasonic techniques for defect detection and condition monitoring in water and sewerage pipes: a review, Appl. Acoust. 183 (2021) 108282.
[4] R. Worley, Y. Yu, S. Anderson, Acoustic echo-localization for pipe inspection robots, in: Proceedings of the 2020 IEEE International Conference on Multisensor Fusion and Integration for Intelligent Systems (MFI), IEEE, Karlsruhe, GermanyNew York, 2020.
[5] Y. Yu, R. Worley, S. Anderson, K.V. Horoshenkov, Microphone array analysis for simultaneous condition detection, localization, and classification in a pipe, J. Acoust. Soc. Am. 153 (367) (2023) 367–383.
[6] Y. Yu, K.V. Horoshenkov, S. Tait, Microphone array analysis of the first non-axisymmetric mode for the detection of pipe conditions, J. Acoust. Soc. Am. 150 (1) (2024) 575–587.
[7] T. Graf, J. Pan, Determination of the complex acoustic scattering matrix of a right-angled duct, J. Acoust. Soc. Am. 134 (1) (2013) 292–299.
[8] C.W. Hsu, B. Zhen, A.D. Stone, J.D. Joannopoulos, M. Soljačić, Bound states in the continuum, Nat. Rev. Mater. 1 (9) (2016) 1–13.
[9] S. Hein, W. Koch, Acoustic resonances and trapped modes in pipes and tunnels, J. Fluid Mech. 605 (2008) 401–428.
[10] C.M. Linton, M. McIver, Trapped modes in cylindrical waveguides, Q. J. Mech. Appl. Math. 51 (1998) 389–412.
[11] D.N. Maksimov, A.F. Sadreev, A.A. Lyapina, A.S. Pilipchuk, Coupled mode theory for acoustic resonators, Wave Motion 56 (2015) 52–66.
[12] A.A. Lyapina, D.N. Maksimov, A.S. Pilipchuk, A.F. Sadreev, Bound states in the continuum in open acoustic resonators, J. Fluid Mech. 780 (2015) 370–387.
[13] Y. Tong, J. Pan, Modal analysis of the scattering coefficients of an open cavity in a waveguide, Wave Motion 68 (2017) 242–252.
[14] A.A. Lyapina, A.S. Pilipchuk, A.F. Sadreev, Trapped modes in a non-axisymmetric cylindrical waveguide, J. Sound Vib. 421 (2018) 48–60.
[15] R. Kirby, Modeling sound propagation in acoustic waveguides using a hybrid numerical method, J. Acoust. Soc. Am. 124 (4) (2008) 1930–1940.
[16] W. Duan, R. Kirby, J. Prisutova, K.V. Horoshenkov, On the use of power reflection ratio and phase change to determine the geometry of a blockage in a pipe, Appl. Acoust. 87 (2015) 190–197.
[17] R. Se-gon, H.R. Choi, Differential-drive in-pipe robot for moving inside urban gas pipelines, IEEE Trans. Robot 21 (1) (2005) 1–17.
[18] P.M. Morse, K.U. Ingard, Theoretical Acoustics, Princeton University Press, 1986.
[19] Y. Yu, A. Krynkin, K.V. Horoshenkov, The effect of 3D surface roughness on acoustic wave propagation in a cylindrical waveguide, Wave Motion 103304 (2024).
[20] L. Jing, Z. Li, Y. Li, R.D. Murch, Channel characterization of acoustic waveguides consisting of straight gas and water pipelines, IEEE Access 6 (2018) 6807–6819.
[21] H. Feshbach, Unified theory of nuclear reactions, Ann. Phys. 5 (1958) 357–390.
[22] P. Morse, H. Feshbach, Methods of Theoretical Physics, 1, McGraw-Hill, New York, 1953.
[23] D.S. Jones, Acoustic and Electromagnetic Waves, Oxford, New York, 1986.
[24] Y. Yu, A. Krynkin, Z. Li, K.V. Horoshenkov, Analytical and empirical models for the acoustic dispersion relations in partially filled water pipes, Appl. Acoust. 179 (2021) 108076, 0003-682X.
[25] "iRobot," Available: www.irobot.com. (Accessed 21 March 2024).
[26] ICAIR, "The Integrated Civil and Infrastructure Research Centre," University of Sheffield, Available: https://www.icair.ac.uk/. (Accessed 21 March 2024).